IEEE Access
Multidisciplinary | Rapid Review | Open Access Journal

Received August 10, 2021, accepted August 25, 2021, date of publication August 30, 2021, date of current version September 8, 2021.

Digital Object Identifier 10.1109/ACCESS.2021.3108638

The Measurement of PSF Ellipticity of an Unobstructed Off-Axis Space Telescope: Error Analysis

KUO FAN[1,2], JING LUO[1], XU HE[1], CHENGHAO LI[1], AND XIAOHUI ZHANG[1]
[1]Changchun Institute of Optics, Fine Mechanics and Physics, Chinese Academy of Sciences, Changchun 130033, China
[2]University of Chinese Academy of Sciences, Beijing 100049, China

Corresponding authors: Jing Luo (luojingopt@ciomp.ac.cn) and Xiaohui Zhang (zhangxiaohui0123@163.com)

This work was supported in part by the National Natural Science Foundation of China under Grant 12003033 and Grant 61875190.

ABSTRACT It is an effective method to detect weak gravitational lensing (WL) in the universe by measuring ellipticities of galaxies via astronomical telescopes. Optical properties of telescopes are critical to WL detections. To ensure the used telescopes to be competent, it is necessary to measure point spread function (PSF) ellipticities of telescopes in labs. In this paper, a way based on simulated star target imaging is proposed to measure PSF ellipticity of an unobstructed off-axis space telescope. Related errors are identified and modeled carefully for the first time. Effects of detector noises, micro-vibration of optical platforms, defocusing of simulated star target, wavefront errors (WFEs) and central obstructions of collimators on PSF ellipticity measurements of the telescope are analyzed. Results show that the measurement error of PSF ellipticity decreases from 0.0105 to 0.0043 by adopting 10 iterations of the iterative weighted centroiding algorithm when SNRs are under 24 dB. To ensure PSF ellipticity measurement errors are not larger than 0.01, the micro-vibration angle of the optical platform should be less than $0.05''$. When focal length of the collimator is twice that of the telescope, the measurement errors of PSF ellipticity are under 0.01 if the defocusing of simulated star target is controlled to be not larger than 0.1 mm. In addition, WFEs and central obstructions of collimators change PSF ellipticity measurement errors to different degrees at different fields of view (FOVs). Due to 20 nm RMS WFE of the collimator, the maximum value of PSF ellipticity measurement errors over full FOVs is 0.1 and the average value is 0.0269. If the radius of central obscuration of the collimator is 150 mm, the maximum measurement error of PSF ellipticity over full FOVs is 0.0091. According to the results shown in this paper, significant references for high accuracy measurements of PSF ellipticity of telescopes can be provided.

INDEX TERMS Weak gravitational lensing, unobstructed off-axis space telescope, PSF ellipticity measurements, error analysis.

I. INTRODUCTION

Weak gravitational lensing (WL) is a slight deflection of the light from background galaxies through a gravitational field formed by dark matter and ordinary matter [1]. WL is a good probe to study dark matter and dark energy in the universe so that it becomes one of the most powerful tools for cosmologists. WL enables to map dark matter and detect dark energy by statistically quantifying the shear distortions encoded in the observed shapes of background galaxies, namely, galaxy ellipticities [2]–[4]. Thus, precisely obtaining ellipticities of galaxies via astronomical telescopes is critical to WL detections [5].

However, ellipticities of galaxies are typically distorted only approximately 1% in size by WL [6], [7]. It is a big challenge to measure such tiny WL signals. Currently, the distortions and unbiased estimates of galaxy shapes are accessed by statistically averaging a very large number of samples [8], [9]. Several large-scale sky survey projects have been proposed successively, including Euclid Space Telescope [10], Nancy Grace Roman Space Telescope [11], Vera C. Rubin Observatory Legacy Survey of Space and Time (LSST) [12], and China Space Station Telescope (CSST) [13]. These telescopes restrain statistical errors to be

The associate editor coordinating the review of this manuscript and approving it for publication was Sukhdev Roy.

small enough [14], [15]. As a result, systematic errors in the measurements of galaxy ellipticities become crucial [16]. The atmosphere is one of the most important errors for ground-based telescopes [17]. By contrast, space telescopes have important advantages. Euclid Space Telescope, Nancy Grace Roman Space Telescope, and CSST are space telescopes.

Since the shapes of galaxies must be convolved by point spread function (PSF) of telescopes before we observe them, optical properties of telescopes are important systematic errors in WL detections [18], [19]. Hence, more comprehensive knowledges of the properties of telescopes are helpful to improve the accuracy of WL detections [20]. An off-axis space telescope for detecting WL is designed by Zhang *et al.* [21]. The smooth PSF ellipticity map of an unobscured telescope to achieve strict constraints on its spatial stability is achieved, and PSF ellipticity is used to evaluate the image quality. Luo *et al.* [22] have analyzed the impacts of polarization aberrations on PSF ellipticity of telescopes via polarization ray tracing. Polarization aberrations of telescopes are non-negligible in WL detections. Zeng *et al.* [23] have studied the influences of geometric aberrations on PSF ellipticity. Monte Carlo simulations have been done for PSF ellipticity to guide the precise alignment of an off-axis telescope.

PSF ellipticities of telescopes depend on many factors, such as optical design, manufacturing errors, optical alignment, and so on. Hence, there may be big differences between the actual performances of PSF ellipticity of telescopes and those in design status. To ensure the used telescopes to be competent in WL detections, it is very necessary to measure PSF ellipticities of telescopes in labs. Currently, PSF measurements of telescopes have been studied widely. PSF of space camera based on wavefront sensing has been estimated by Li *et al.* [24]. They have calculated PSF using Fourier transformation of pupil function which is constructed by wavefront errors (WFEs). Karcher *et al.* [25] and Takacs *et al.* [26] measure the edge response function and carry on the Gauss curve fitting to obtain PSF of the optical system. The team of Euclid Space Telescope [27] has proposed a method based on source plate imaging to measure PSFs. The source plate consists of a flat fused silica plate with inserted single-mode optical fibers at 22 positions along the FOVs. PSF has been obtained by indirect interference fringe method that measures the modulation transfer function (MTF) directly by Andersen and Sorensen *et al.* [28]. PSF could be derived from the MTF by Fourier transformation. However, PSF ellipticity measurements of telescopes have not been involved in the aforementioned works. Error sources that dominate PSF ellipticity measurements are very different from those in traditional PSF measurements. For example, the non-rotationally symmetrical WFEs have greater impacts on PSF ellipticity measurements. In addition, some new errors should be considered.

In this paper, we will focus our attentions on PSF ellipticity measurement of an unobstructed off-axis space telescope that is designed to detect WL in space. According to the error budget of the telescope, measurement errors of PSF ellipticity should be smaller than 0.01. A way based on simulated star target imaging is proposed. Related errors are identified and modeled carefully. It should be mentioned that galaxy ellipticity measurements have been analyzed by Chang *et al.* [15] and Richard [20] and Okura *et al.* [29] and Okura and Futamase [30]–[32]. However, these studies are very different from this paper. Firstly, the meaning of galaxy ellipticity is different from that of PSF ellipticity of telescopes. Galaxy ellipticity characterizes the shape of a galaxy. As contrast, PSF ellipticity belongs to optical properties of telescopes and is a critical error source in galaxy ellipticity measurements. Secondly, their purposes are different. The main goal of Chang *et al.* and Okura *et al.* is to get ellipticities of the target galaxies as true as possible. As a contrast, the goal of this study is to obtain optical properties of the telescope as true as possible. Thirdly, their methods are different. In the studies of Chang *et al.* and Okura *et al.*, interpolating or weighting multiple brighter stars is proposed to improve the measurement accuracy of background galaxy ellipticity. In this study, we adopt a method in which fields of view (FOVs) of a single simulated star target is changed to measure PSF ellipticity of the telescope on the ground. Obviously, bright stars are good enough sources for telescope calibrations. However, they are only available in orbit. It is so difficult to get a qualified collimated beam that can fill a 2m entrance pupil in labs. Last but not least, the related errors differ. In the studies by Chang *et al.*, counting statistics, tracking errors and atmosphere distortions are significant. Of course, nonideal optical properties of telescopes are also mentioned. However, they are analyzed via simulations. Moreover, the systematic error generated by photon noise which is Poisson noise of flux from the atmosphere is considered by Okura *et al*. In this paper, we devote to measure PSF ellipticity of our telescope in the lab instead of simulation. There would be important differences between simulation results and actual performances of the telescopes. What is more, the atmosphere, which is one of the most important errors in the studies of Chang *et al.* and Okura *et al.* would not be considered at all in this paper. According to our scheme, a collimator would be used to fill the entrance pupil with a 2 m aperture of the telescope, which would induce many errors. Laboratory environment, measurement scheme, defocusing of simulated star target, WFEs and central obscurations of collimators are critical errors and would be analyzed very carefully in this paper. In fact, to the best of our knowledge, it is the first time to measure PSF ellipticities of telescopes in labs and the related errors are analyzed.

The rest of this paper is arranged as follows. Definition and calculation accuracy analysis of PSF ellipticity of telescopes are shown in Section 2. In Section 3, we introduce PSF ellipticity characteristics of an unobstructed off-axis telescope, and show a PSF ellipticity measurement method of the telescope. Errors affecting the measurement of PSF ellipticity of the telescope are analyzed in Section 4. Some conclusions are summarized in Section 5.

II. PSF ELLIPTICITY

A. DEFINITION OF PSF ELLIPTICITY

PSF is the impulse response of an optical system. PSF characterizes the intensity distribution of the diffraction pattern emitted from an infinitely small point source passing through the system. PSF can be defined by [33]

$$PSF = |\mathcal{F}\{P\}|^2, \quad P = Ae^{\left(\frac{2\pi i\Delta}{\lambda}\right)}, \tag{1}$$

where P means the pupil function, λ is the wavelength of light, A indicates the aperture function, and Δ is the optical path difference. Aperture function A and optical path difference Δ are two major parameters that dominate the characteristics of PSFs of optical systems.

PSF ellipticity is a parameter to characterize the shape and spatial distribution of PSF [5]. Let $\Phi(x, y)$ be the light intensity of an image, centroids of images are given by the weighted first order moments divided by the total intensity

$$\begin{cases} \bar{x} = \dfrac{\int \Phi(x,y)\, W(x,y)\, x dxdy}{\int \Phi(x,y)\, W(x,y)\, dxdy} \\ \bar{y} = \dfrac{\int \Phi(x,y)\, W(x,y)\, y dxdy}{\int \Phi(x,y)\, W(x,y)\, dxdy}, \end{cases} \tag{2}$$

where $W(x, y)$ is a weight function used to depress noise. The quadrupole moment matrix is given by the weighted second moments divided by the total intensity

$$\begin{cases} Q_{XX} = \dfrac{\int \Phi(x,y)\, W_o(x,y)\, (x-\bar{x})^2\, dxdy}{\int \Phi(x,y)\, W_o(x,y)\, dxdy} \\ Q_{XY} = \dfrac{\int \Phi(x,y)\, W_o(x,y)\, (x-\bar{x})\,(y-\bar{y})\, dxdy}{\int \Phi(x,y)\, W_o(x,y)\, dxdy} \\ Q_{YY} = \dfrac{\int \Phi(x,y)\, W_o(x,y)\, (y-\bar{y})^2\, dxdy}{\int \Phi(x,y)\, W_o(x,y)\, dxdy}. \end{cases} \tag{3}$$

where $W_o(x, y)$ means a Gaussian weight function of the scale length, which is some measure of PSF size such as the half-light radius.

PSF ellipticity e has two components, namely, e_1 and e_2, which are defined from the weighted second moments Q_{xx}, Q_{xy}, Q_{yy} of PSF. They can be written using Eq. (3) as follows:

$$\begin{cases} e_1 = \dfrac{(Q_{xx} - Q_{yy})}{(Q_{xx} + Q_{yy})} \\ e_2 = \dfrac{2Q_{xy}}{(Q_{xx} + Q_{yy})}, \end{cases} \tag{4}$$

and PSF ellipticity e is represented by the two components [34]

$$e = \sqrt{e_1^2 + e_2^2}. \tag{5}$$

B. CALCULATION ACCURACY OF PSF ELLIPTICITY

Exact calculation of PSF ellipticity is critical to analyze PSF ellipticities of telescopes. According to the definition of PSF ellipticity, its value depends on PSF sampling, including pupil sampling and image sampling [35]. Pupil sampling indicates the sampling accuracy of the pupil function, which determines the accuracy of PSF. Image sampling means the sampling accuracy of PSF of an image, which determines the calculation accuracy of PSF ellipticity. The connection between pupil sampling and image sampling is [36]

$$GRI = \frac{\lambda \times f/d \times NDR}{TGR}, \tag{6}$$

where GRI means the grid spacing between samples in the image plane, which indicates the image sampling spacing in mm; NDR is the number of rays across the pupil diameter; TGR means the total number of rays across the transform grid; λ is the wavelength of light; f/d is the F-number.

Pupil sampling interval is inversely proportional to image sampling interval due to the limitation of the simulation ability. Specifically, larger image sampling interval increases the number of pupil sampling and decreases pupil sampling interval. The calculation accuracy of PSF ellipticity includes two primary aspects: relative calculation accuracy and interpolation accuracy [23]. The relationship between pupil sampling and image sampling shows that larger number of pupil sampling achieves higher calculation accuracy of PSF ellipticity. Thus, differences between the results derived by a higher pupil sampling number and those by a lower one can be used to evaluate the relative calculation accuracy of PSF ellipticity. The analyses about the PSF ellipticity calculation accuracy of Euclid Space Telescope points out the full FOVs PSF ellipticity interpolation errors should be less than 2.00e-4. It is the main reference when we calculate PSF ellipticity.

To balance the accuracy and efficiency of PSF ellipticity calculation [23], a 2048 × 2048 matrix with 0.4 microns image sampling interval is chosen in this paper. PSF ellipticity is obtained in a 67.9 microns (0.5″) radius circle centering in the centroid of each PSF. The relative calculation accuracy of PSF ellipticity is 1.00e-4, and the interpolation accuracy is 1.31e-4, which meet the requirement of our telescope.

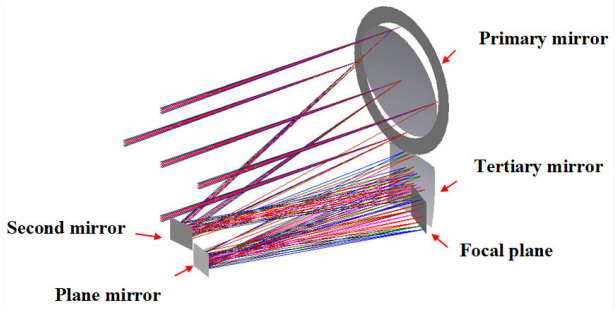

FIGURE 1. The optical layout of an unobstructed off-axis telescope.

III. THEORY OF PSF ELLIPTICITY MEASUREMENTS

A. AN UNOBSTRUCTED OFF-AXIS SPACE TELESCOPE

The telescope analyzed in this paper is designed to detect WL in space. It has superior optical performances. The optical layout of the telescope is shown in Fig. 1. It is a Cook type three-mirror anastigmatic (TMA) telescope with a 2 m

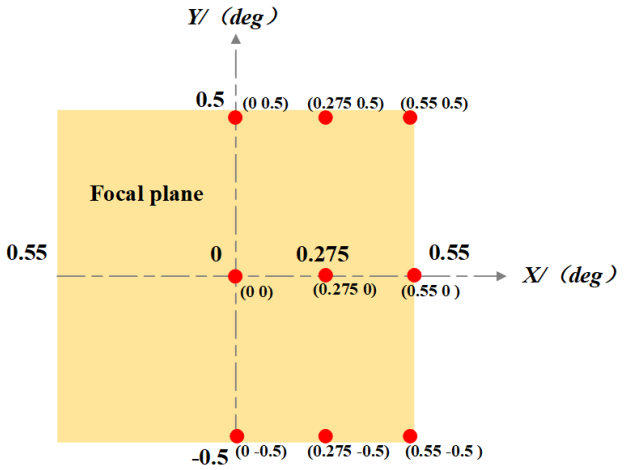

FIGURE 2. Schematic diagram of the nine FOVs of (0/0.275/0.55, 0.5/0/−0.5)° of the telescope.

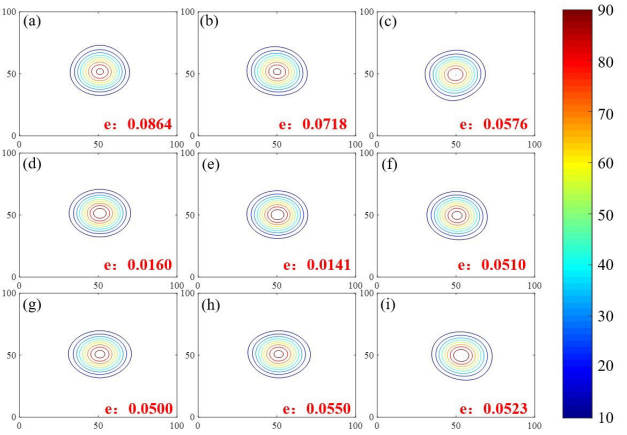

FIGURE 3. The shape and spatial distribution of PSFs and corresponding PSF ellipticities in the nine FOVs.

aperture, 28 m focal length, and $1.1 \times 1°$ FOVs [21]. Over full FOVs, the RMS WFEs are smaller than 0.055 λ, the EE80 (80% Encircled Energy) radiuses of PSFs are less than 0.13″, and PSF ellipticities are not greater than 0.15 [23]. The telescope is symmetric about YOZ plane. Hence, the nine FOVs of (0/0.275/0.55, 0.5/0/−0.5)° located in the half plane $x > 0$ (as shown in Fig. 2) are chosen to show the shape and spatial distribution of PSFs and corresponding PSF ellipticities, as shown in Fig. 3.

B. AN METHOD USED TO MEASURE PSF ELLIPTICITY

According to the astronomical applications of the telescope, a method based on simulated star target imaging is proposed to measure PSF ellipticity. The measurement scheme is shown in Fig. 4. The optical layout is composed of an incoherent illumination system, a star target simulator including a narrow bandpass filter of 632.8 nm and a star hole, a collimator, a multidimensional adjustment platform, a telescope, and an image acquisition system. The exit pupil of the collimator matches the entrance pupil of the telescope. Due to the manufacturing difficulty and cost of collimators, a collimator whose aperture is 2 m, which is identical to the telescope is chosen. The infinity simulated star target with $\lambda = 632.8\ nm$ is achieved by the incoherent illumination system, the star target simulation system and the collimator, and is imaged onto the focal plane of the telescope finally. PSF of a telescope depends on wavelength directly. In this paper, the light whose wavelength is 632.8 nm is chosen. Different FOVs of the telescope are switched via the multi-dimensional adjustment platform. The image acquisition system consists of a microscope and a detector. According to the ability of the detector in the lab, a detector with a pixel size of 4 microns is adopted. To restrain the coupling effects between PSF ellipticity calculation errors and other errors, a microscope with 10× magnification is placed in front of the detector. As a result, the image is magnified 10 times by the microscope and the detector pixel is subdivided to 0.4 microns.

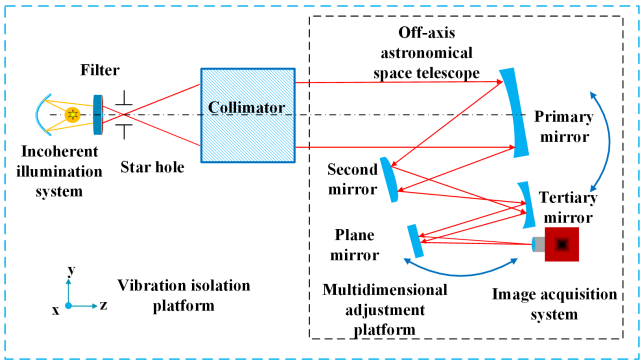

FIGURE 4. Schematic diagram of optical path to measure PSF ellipticity of an unobstructed off-axis telescope.

IV. ERROR ANALYSIS

According to the error budget of the telescope, the requirements about PSF ellipticity are as follows: over full FOVs, the maximum value of PSF ellipticities should be less than 0.15, the average value cannot be larger than 0.05 [23]. Hence, the measurement errors of PSF ellipticity over all FOVs are required to be less than 0.01 in the lab. In order to ensure that our PSF ellipticity measurement scheme (as shown in Fig. 4) meets the requirements, related errors are identified.

The main errors are summarized as follows:

(1) Centroid positioning errors of PSFs;
(2) Micro-vibration of optical platforms;
(3) Defocusing of simulated star target;
(4) WFEs of collimators;
(5) Central obscurations of collimators.

Next, these errors will be carefully analyzed one by one.

A. CENTROID POSITIONING ERRORS OF PSFs

According to the definition of PSF ellipticity, as shown by Eqs. (2)-(5), the centroids of images are vital factors

contributing to PSF ellipticity measurements because they determine the area involved in the PSF ellipticity calculation. However, noise of detectors would induce centroid positioning errors.

Detector noise can be characterized by the amplitude distribution following the Gaussian distribution and the power spectral density following the uniform distribution. The probability density function is expressed by [37]:

$$f(\varepsilon) = \frac{1}{\sqrt{2\pi}\sigma} \exp\left(-\frac{(\varepsilon-\mu)^2}{2\sigma^2}\right), \tag{7}$$

where μ is the mathematical expectation, and σ^2 denotes the variance.

In this paper, an iterative weighted centroiding algorithm [38] is used to reduce impacts of detector noise. Weight function is assigned to different pixels of images to reduce effects of marginal pixels with low SNR [39]. Gaussian function $W(x, y)$ is as the weight function [40]

$$W(x, y) = \frac{1}{2\pi\sigma_x\sigma_y} \exp\left[-\frac{(x-\bar{x})^2}{2\sigma_x^2} - \frac{(y-\bar{y})^2}{2\sigma_y^2}\right]. \tag{8}$$

The zero moment S and the first moments S_x, S_y of the image intensity are shown as:

$$S = \int \Phi(x, y)\, W(x, y)\, dxdy, \tag{9}$$

$$\begin{cases} S_x = \left(\frac{1}{S}\right) \int x\Phi(x, y)\, W(x, y)\, dxdy \\ S_y = \left(\frac{1}{S}\right) \int y\Phi(x, y)\, W(x, y)\, dxdy. \end{cases} \tag{10}$$

Similarly, the second moments S_{xx} and S_{yy} can be obtained by:

$$\begin{cases} S_{xx} = \left(\frac{1}{S}\right) \int x^2\Phi(x, y)\, W(x, y)\, dxdy \\ S_{yy} = \left(\frac{1}{S}\right) \int y^2\Phi(x, y)\, W(x, y)\, dxdy. \end{cases} \tag{11}$$

We can get the Gaussian widths of the Gaussian weight function, namely, σ_x and σ_y

$$\begin{cases} \sigma_x = \sqrt{S_{xx}S - S_x^2} \\ \sigma_y = \sqrt{S_{yy}S - S_y^2}, \end{cases} \tag{12}$$

and the centroids $\bar{x}$ and $\bar{y}$ of the image

$$\begin{cases} \bar{x} = S_x \\ \bar{y} = S_y. \end{cases} \tag{13}$$

Eventually, we substitute the Gaussian widths and centroids calculated from Eqs. (12) and (13) into Eq. (8). Iterations are performed until the centroid positioning accuracy is satisfied.

According to the common level of detectors used in astronomy [41], we simulate the image with a SNR of 30 dB. With the iterative weighted centroiding algorithm, centroid positioning and PSF ellipticity measurement errors along with increasing iterations are obtained. Results are shown in Figs. 5(a) and 5(b), respectively. The curves appear steep in the first 10 iterations. As the number of iterations increases, the errors of both centroid positioning and PSF ellipticity measurement gradually decrease. However, from 10 to 30 iterations, the curves seem quite smooth. In this case, the changes in centroid positioning errors in x and y directions and PSF ellipticity measurement error are 2.31e-4, 3.52e-4, and 4.84e-5, respectively. In terms of the results shown in Fig. 5, 10 iterations are adopted for the iterative weighted centroiding algorithm. It is found that the centroid positioning errors in the x and y directions are 1.56e-2 and 1.98e-2, and the PSF ellipticity measurement error is 1.64e-3.

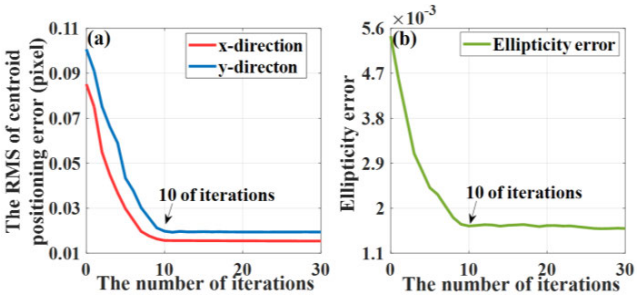

FIGURE 5. Relation of the number of iterations with the errors of (a) centroid positioning and (b) PSF ellipticity measurement.

To verify performances of the iterative weighted centroiding algorithm, SNR range of the image is set from 20 dB to 40 dB. In this case, the errors of centroid positioning and PSF ellipticity measurement with and without the iterative weighted centroiding algorithm are calculated and compared. Results are shown in Figs. 6(a) and 6(b), respectively. As shown in Fig. 6(a), the centroid positioning errors in x and y directions without the iterative weighted centroiding algorithm are larger than 3.94e-1 and 3.76e-1 when SNRs are less than 24 dB. Meanwhile, the measurement errors of PSF ellipticity are greater than 0.01, as shown in Fig. 6(b). However, when the iterative weighted centroiding algorithm with 10 iterations is used, the centroid positioning errors in x and y directions reduce to 4.78e-2 and 4.83e-2, and the PSF ellipticity measurement error reduces to 4.32e-3. Therefore, the iterative weighted centroiding algorithm enables to effectively reduce PSF ellipticity measurement errors from detector noise.

B. MICRO-VIBRATION OF OPTICAL PLATFROMS

In the process of image acquisition, micro-vibration of optical platform leads to image offset from optical axis. Accumulated offsets would alter the shape of PSF, resulting in inaccurate PSF ellipticity measurement. Micro-vibration angles of optical platforms are random. The image offsets caused by the micro-vibration can be described by a Gaussian distribution function [42]. The PSF suffered from micro-vibration $PSF(x, y)_m$ is the convolution of no micro-vibration

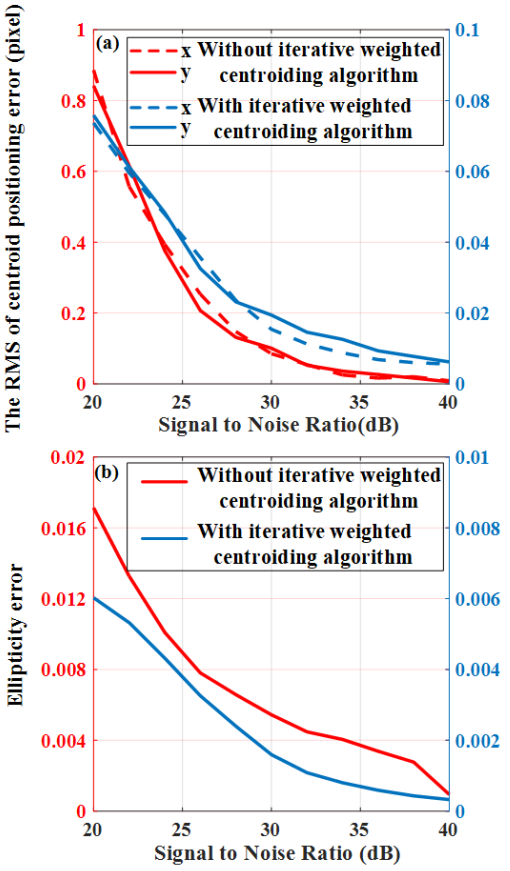

FIGURE 6. The errors of (a) centroid positioning and (b) PSF ellipticity measurement at different SNRs with and without the iterative weighted centroiding algorithm.

$PSF(x, y)$ and Gaussian function $Gauss(x, y)$

$$PSF(x, y)_m = PSF\ (x, y) * Gauss\ (x, y)\ . \tag{14}$$

Monte Carlo simulations are performed to analyze the influences of different micro-vibration angles on PSF ellipticity measurement of the telescope. Fig. 7 shows that the measurement errors of PSF ellipticity and their occurrence probability. When micro-vibration angles are not greater than $0.05''$, the measurement errors of PSF ellipticity are less than 0.01, as shown in Figs. 7(a)–7(c). If micro-vibration angles are up to $0.06''$, PSF ellipticity measurement errors are under 0.01 with probability of 45%, as shown in Fig. 7(d). Once micro-vibration angles exceed $0.085''$, the measurement errors of PSF ellipticity are greater than 0.01, as shown in Figs. 7(e)–7(f).

For obtaining the measurement errors of PSF ellipticity at different FOVs, simulations are performed in the nine FOVs of $(0/0.275/0.55,\ 0.5/0/-0.5)°$. Results are shown in Table 1. Although the PSF ellipticity measurement errors differ at different FOVs, the maximum error is 9.87e-3, which is within the range of the requirement. Therefore, the micro-vibration angles of the optical platform should be controlled to be not greater than $0.05''$ for our system. At present, it has been tested to be less than $0.02''$ [43] in our lab, which can meet the requirement of PSF ellipticity measurement.

C. DEFOCUSING OF SIMULATED STAR TARGET

Defocusing itself and its combined effects with some aberrations would alter PSF [23]. To improve measurement accuracy of PSF ellipticity of the telescope in the lab, defocusing of simulated star target should be considered and the focal length of collimators should be selected reasonably. The focal length of our telescope is 28 m. The focal length of the collimator is assumed to be 28 m, 56 m, and 84 m, respectively. Considering calibrations level of the focal plane of general collimators with large aperture and long focal length [44]–[47], defocusing of simulated star target is set to be 0.2 mm. Collimators with different focal lengths are analyzed, and variations of PSF ellipticity of the telescope in the central FOV of $(0, 0)°$ and marginal FOV of $(0, 0.5)°$ suffered from defocusing of simulated star target are obtained, as shown in Figs. 8(a)–8(c). It can be seen that increasing defocusing of simulated star target increases the measurement errors of PSF ellipticity. What is more, influences of defocusing at the marginal FOV are larger those at the center FOV.

When the focal length of the collimator is identical to that of the telescope measured, i.e., 28 m, the results are shown in Fig. 8(a). The measurement errors of PSF ellipticity caused by defocusing of simulated star target are significant, the maximum measurement errors of PSF ellipticity in the central and marginal FOVs are 0.0436 and 0.0975, respectively. Currently, the calibration error of focal length of large aperture collimators is about 0.1mm, in this case, the measurement errors of PSF ellipticity in the two FOVs are 0.0213 and 0.0511, which are larger than the requirement of 0.01. Hence, a collimator with the same focal length as the telescope is not suitable for measuring PSF ellipticity.

When the focal length of the collimator is up to 56 m, the results are shown in Fig. 8(b). The maximum measurement errors of PSF ellipticity in the center and marginal FOVs induced by defocusing of simulated star target become 0.0123 and 0.0241, respectively. Obviously, the results are better than those using the collimator whose focal length is 28 m. If defocusing of simulated star target is controlled within 0.1 mm, the measurement errors of PSF ellipticity at the two FOVs are not larger than 0.01. Therefore, the effects of defocusing on measurements of PSF ellipticity can be effectively reduced by adopting a collimator whose focal length is twice that of the telescope.

When the focal length of the collimator is triple that of the telescope, the results are shown in Fig. 8(c). The maximum measurement errors of PSF ellipticity induced by defocusing of simulated star target are 0.0053 and 0.01 in the center and marginal FOVs, which are smaller than those in Fig. 8(b). However, the collimator with such a long focal length is really hard to developed. Hence, a collimator that is twice the focal length of the telescope is preferred.

For obtaining the measurement errors of PSF ellipticity over other FOVs, the relationships between measurement

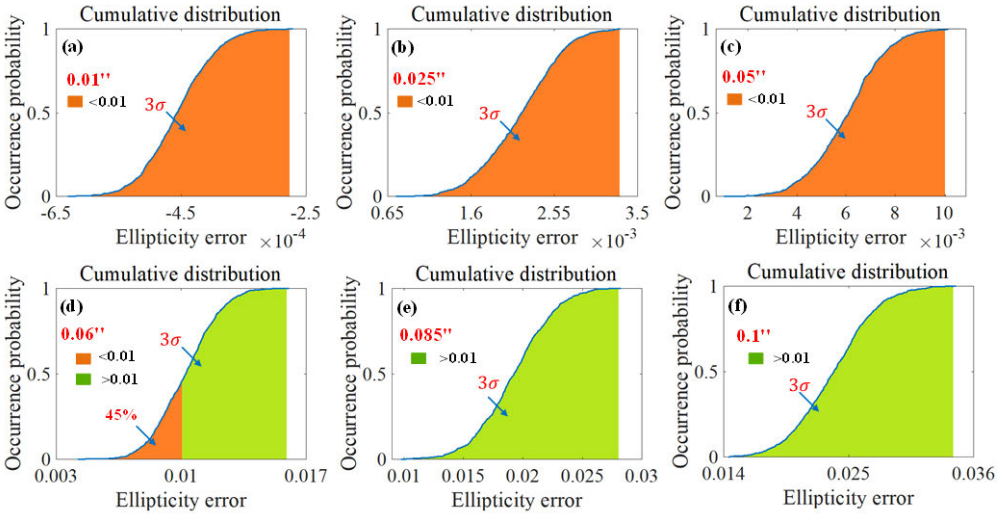

FIGURE 7. PSF ellipticity measurement errors with different micro-vibration angles.

TABLE 1. PSF ellipticity measurement errors of the nine FOVs at 0.05″ micro-vibration angle.

FOVs	1	2	3	4	5	6	7	8	9
Errors(3σ) ×10-3	9.36	9.04	9.56	6.52	9.52	9.73	9.87	9.84	9.47

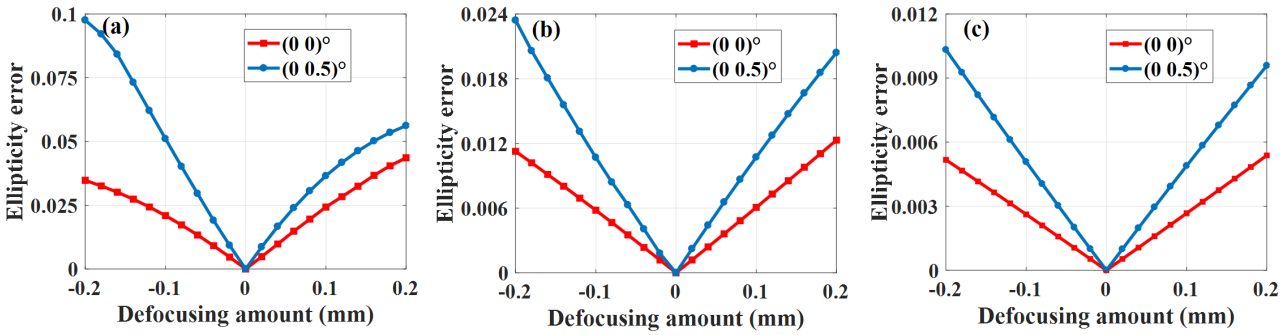

FIGURE 8. PSF ellipticity measurement errors with defocusing of simulated star target when collimator focal length of (a) 28 m (b) 56 m (c) 84 m.

TABLE 2. The relationships between the measurement errors of PSF ellipticity and defocusing of simulated star target in the nine FOVs.

FOVs / Defocusing	1	2	3	4	5	6	7	8	9
-0.2 mm	0.0241	0.0272	0.0295	0.0112	0.0094	0.0207	0.0210	0.0191	0.0274
-0.1 mm	0.0098	0.0089	0.0098	0.0058	0.0048	0.0071	0.0068	0.0062	0.0093
0.1 mm	0.0100	0.0087	0.0097	0.0060	0.0050	0.0072	0.0067	0.0061	0.0092
0.2 mm	0.0204	0.0255	0.0278	0.0123	0.0101	0.0222	0.0195	0.0178	0.0271

errors of PSF ellipticity and defocusing of simulated star target in the nine FOVs are shown in Table 2. Obviously, they are all within the range of the requirement when defocusing of simulated star target is less than 0.1 mm. Therefore, considering the aforementioned factors and the control ability of defocusing of simulated star target in our lab, a collimator that is twice the focal length of the telescope would be selected for PSF ellipticity measurement.

D. WFEs AND CENTRAL OBSTRUCTIONS OF COLLIMATORS

Bright stars are good enough sources for PSF ellipticity calibrations and are available in orbit. However, it is very difficult to obtain a qualified incoherent collimated beam that can fill a telescope with 2 m diameter. Collimators are good choices, but several other new troubles appear, such as WFEs and central obscurations of collimators.

A strong correlation exists between WFEs and PSF ellipticities of telescopes. Their distributions are very similar to each other over full FOVs [23]. The infinity star target simulated from the collimator enters the optical system and exits from its exit pupil, as shown in Fig. 9. Obviously, the WFE of the collimator would superimpose the WFE of the optical system. As a result, the outgoing WFEs are different from those without the collimator. Hence, the collimator contributes to PSF ellipticity of the whole optical system. According to the definition of PSF, as shown in Eq. (1), the aperture function has significant impacts on the distribution form of PSF [33]. Collimators without central obscurations are best choices for PSF ellipticity measurements. However, considering the difficulty of manufacture, it is really hard to construct such a large aperture, long focal length collimator without a central obscuration. Hence, the effects of central obscurations of collimators on the PSF ellipticity measurements should be analyzed.

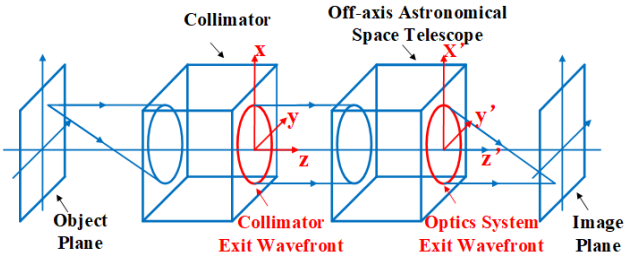

FIGURE 9. Exit pupil relationship model of the collimator and the optical system under testing.

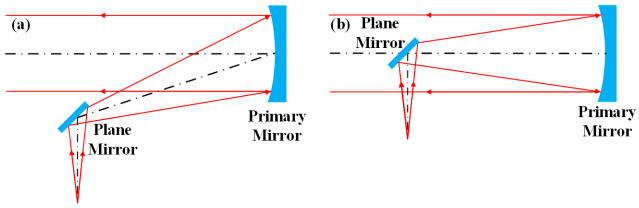

FIGURE 10. Collimators (a) without central obscuration and (b) with central obscuration.

The collimator is a Newton system, which has the same aperture as our telescope and the focal length of 56 m. It is used to simulate an infinity star target. Two kinds of collimators, namely, without central obscuration and with central obscuration, are considered and shown in Figs. 10(a) and 10(b). These effects of WFEs and central obscurations of collimators on PSF ellipticity measurements would be analyzed, respectively.

1) WFEs OF COLLIMATORS

Based on common collimators with 2 m aperture [46]–[48], the RMS WFE of the collimator is assumed to be 20 nm when adopting an unobstructed collimator shown in Fig. 10(a). Given the complexity of actual aberrations of the collimator, each aberration contributes to PSF ellipticity should be considered. The first 36 standard Zernike aberrations one by one are analyzed. Firstly, it is supposed that the collimator contains only one Zernike aberration each time, and its value is 20 nm. The PSF ellipticity measurement errors at the central FOV of (0, 0)° and the marginal FOV of (0, 0.5)° are obtained, and results are shown in Figs. 11(a) and 11(b). It can be seen that variations of PSF ellipticity measurement errors along with different Zernike aberration types are similar between the center FOV and marginal FOV, but the error values are different. The average measurement errors of PSF ellipticity of two FOVs caused by 36 Zernike aberrations are 0.0153 and 0.0273, respectively. Both the maximum values of the two FOVs are less than 0.1. PSF ellipticity is sensitive to low-order aberrations of the collimator from Z4 to Z11. Especially primary astigmatism (Z5 and Z6) and coma (Z7 and Z8) contribute mostly to PSF ellipticity measurement errors. Astigmatism and coma of the marginal FOV have greater influences on PSF ellipticity than those of the center FOV. It is noted that defocusing (Z4) only affects PSF ellipticity at the marginal FOV. For high-order aberrations of the collimator from Z12 to Z36, coma has the largest effects (Z16 and 17 are secondary coma, Z29 and 30 are tertiary coma), followed by astigmatism (Z12 and 13 indicate secondary astigmatism), and other aberrations only cause small variations in measurement errors of PSF ellipticity. What is more, the maximum measurement error of PSF ellipticity in the central FOV caused by the tertiary coma (Z30) is 0.0916.

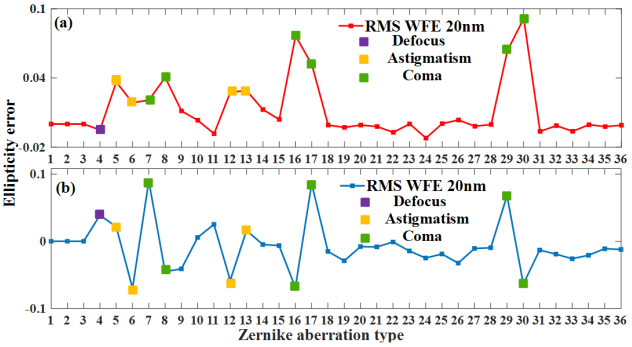

FIGURE 11. PSF ellipticity measurement errors with 36 Zernike aberrations of an unobscured collimator whose RMS WFE of 20 nm: (a) the center FOV of (0 0)°; (b) the marginal FOV of (0 0.5)°.

We simulate the RMS WFEs of the collimator to be 20 nm, 30 nm, and 40 nm. Using the abovementioned methods, the measurement errors of PSF ellipticity in the nine FOVs of (0/0.275/0.55, 0.5/0/−0.5)° are obtained, results as shown in Fig. 12. For the same Zernike aberration type in the same FOV, PSF ellipticity measurement errors are linearly increasing with aberration values. In the nine FOVs, relations between PSF ellipticity measurement errors and different Zernike aberration types are similar. Coma and astigmatism are still the most important aberrations. Defocusing plays a significant role only at marginal FOVs. According to Fig. 12(d), the maximum measurement errors of PSF ellipticity all occur in the central FOVs, which are induced

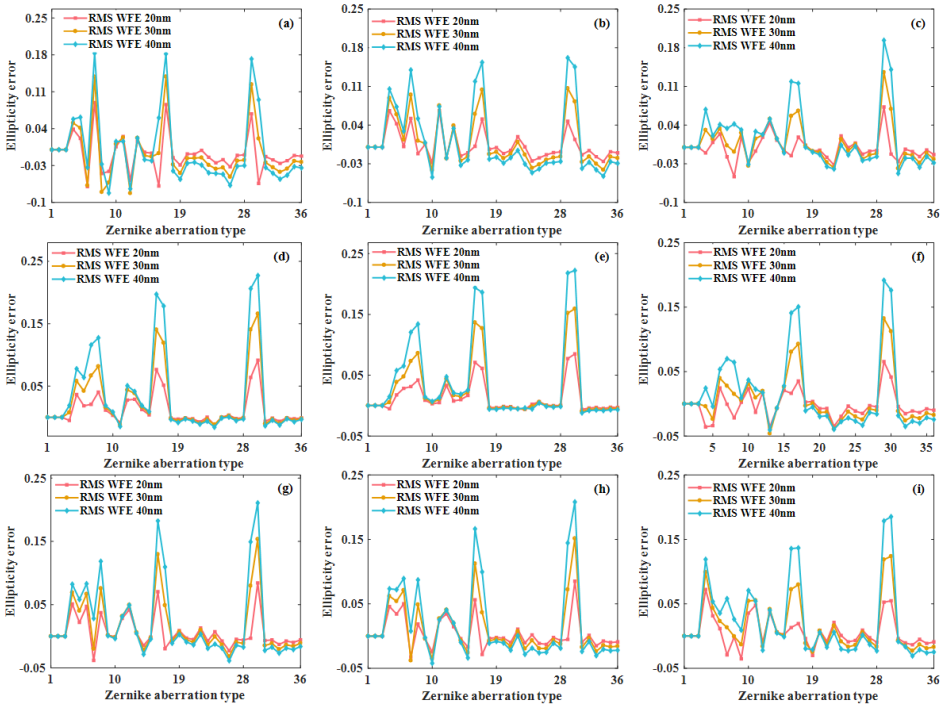

FIGURE 12. PSF ellipticity measurement errors with 36 Zernike aberrations of the unobstructed collimator whose RMS WFEs of 20 nm, 30 nm, and 40 nm in the nine FOVs.

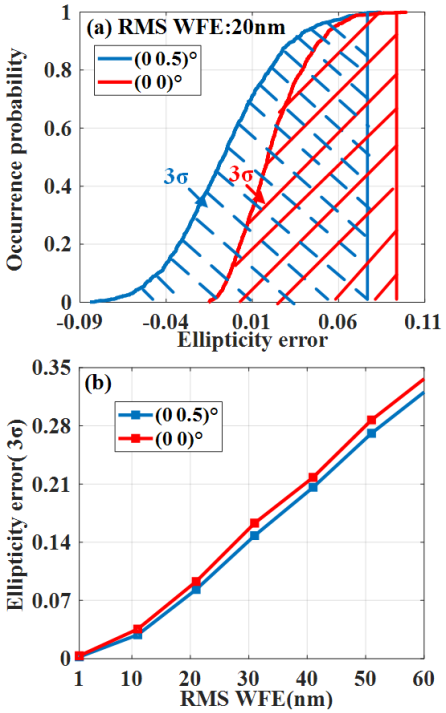

FIGURE 13. PSF ellipticity measurement errors of the center FOV of (0 0)° and the marginal FOV of (0 0.5)° using the unobstructed collimator (a) with the RMS WFE of 20 nm and (b) with the RMS WFEs of 0 nm-60 nm.

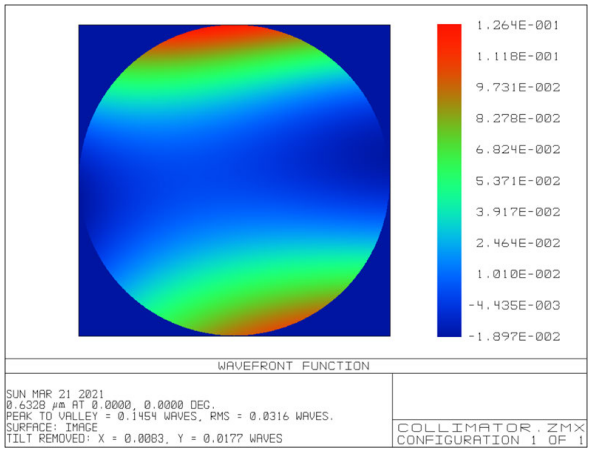

FIGURE 14. Wavefront distribution of the unobstructed collimator whose RMS WFE of 20 nm.

by the tertiary coma (Z30). When the RMS WFEs of the tertiary coma are 20 nm, 30 nm, and 40 nm, the maximum measurement errors of PSF ellipticity are 0.0916, 0.1661, and 0.2273, respectively.

Obviously, WFEs of collimators have big effects on PSF ellipticity measurement. Random combinations of various Zernike aberrations are added to the collimator, and the total RMS WFE keeps to be 20 nm. In this case, the probability distributions of PSF ellipticity measurement errors in the center FOV of (0, 0)° and the marginal FOV of (0, 0.5)° are obtained, results are shown in Fig. 13 (a). Considerable differences can be observed between PSF ellipticity measurement error maps at the two FOVs. Their 3σ values are 0.0976 and 0.0858, respectively. It can be seen that when the RMS WFE of the collimator is 20 nm, the measurement errors of PSF ellipticity are practically within 0.1 regardless of how the

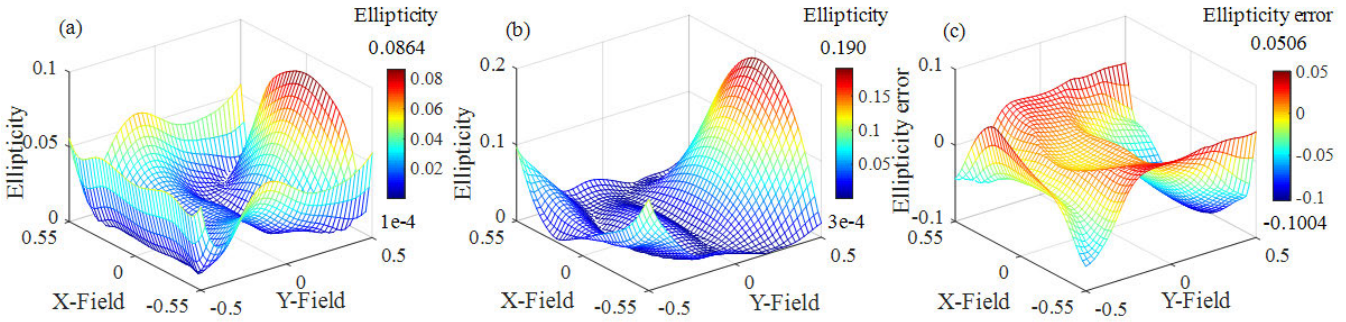

FIGURE 15. PSF ellipticity distributions of the off-axis telescope using the unobscured collimator (a) with the RMS WFE of 0 nm and (b) with the RMS WFE of 20 nm, and (c) the differences of PSF ellipticity of the telescope with the two kinds of WFEs.

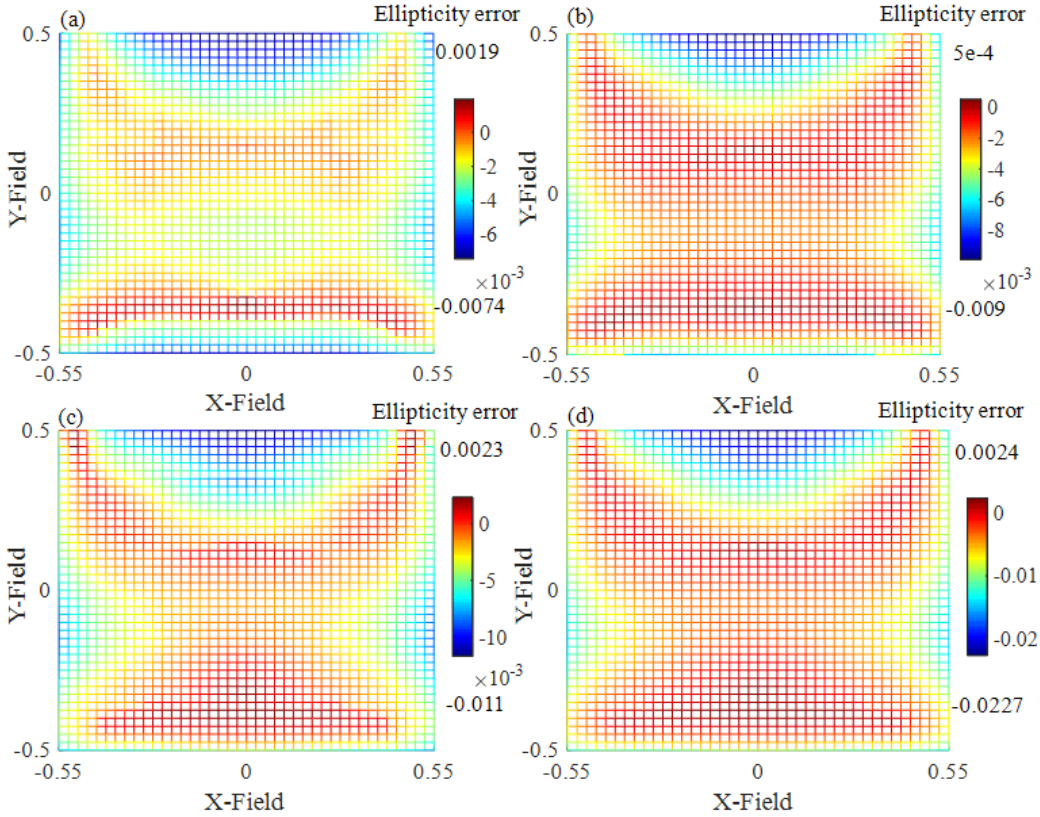

FIGURE 16. PSF ellipticity measurement error distributions of the telescope using the collimator whose RMS WFE of 0 nm with central obstruction radiuses of (a) 100 mm, (b) 150 mm, (c) 200 mm, and (d) 250 mm.

Zernike aberrations are combined. The RMS WFE range of the collimator is altered from 1 nm to 60 nm in a random combination, and 3σ values of PSF ellipticity measurement errors in two FOVs are obtained, as shown in Fig. 13(b). Increasing RMS WFE of the collimator increases the measurement errors of PSF ellipticity. According to Fig. 13(b), 3σ values of PSF ellipticity measurement errors are less than 0.01 only when the RMS WFEs of the collimator are under 3 nm.

PSF ellipticities over full FOVs are critical. The smooth PSF ellipticity distribution is conductive to reduce interpolation errors and to achieve high accuracy in WL detections [49]. Fig. 15(a) shows the PSF ellipticity distribution of the off-axis telescope shown in Fig. 1 over full FOVs of $1.1^\circ \times 1^\circ$ when the collimator is ideal and its RMS WFE is 0 nm. We can see that the PSF ellipticity map is quite smooth. To obtain the effects of RMS WFE of the collimator on PSF ellipticity measurements over full FOVs, the RMS WFE of the collimator is set to be 20 nm. Wavefront distribution of the collimator is shown in Fig. 14. Then, new PSF ellipticity map over full FOVs is shown in Fig. 15(b). Fig. 15(c) shows the differences between Figs. 15(a) and 15(b). We can see that

TABLE 3. PSF ellipticity measurement errors with different central obstruction radiuses of the collimator.

Ellipticity / Collimator	RMS WFE of 0 nm		RMS WFE of 20 nm	
Central Obstruction radius	Average errors	Maximum errors	Average errors	Maximum errors
100 mm	2.29e-3	7.40e-3	3.20e-3	1.36e-2
150 mm	2.75e-3	9.01e-3	4.72e-3	2.04e-2
200 mm	3.17e-3	1.10e-2	7.00e-3	2.70e-2
250 mm	5.56e-3	2.27e-2	1.15e-2	4.57e-2

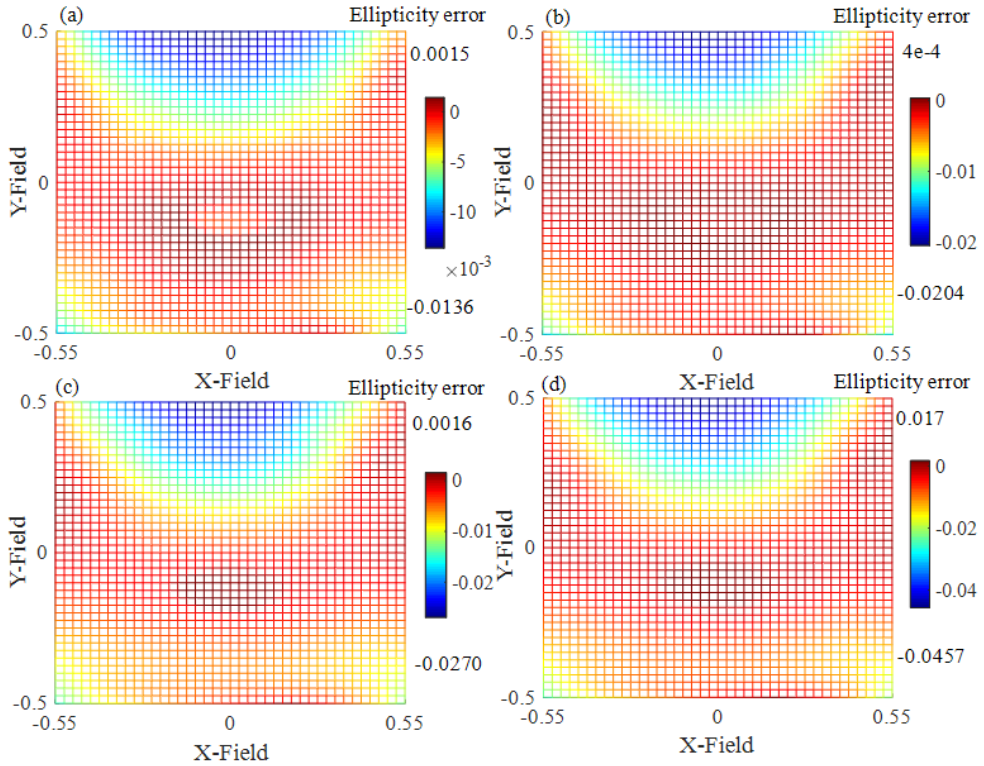

FIGURE 17. PSF ellipticity measurement error distributions of the off-axis telescope using the collimator whose RMS WFE of 20 nm with central obstruction radiuses of (a) 100 mm, (b) 150 mm, (c) 200 mm, and (d) 250 mm.

the differences induced by the WFE of the collimator differ at different FOVs. According to Fig. 15(c), the maximum error of PSF ellipticity is 0.1 and the average value is 0.0269.

2) CENTRAL OBSCURATIONS OF COLLIMATORS

Central obstructions of collimators have significant impacts on PSF [50]. The collimator with central obscuration analyzed in this paper is shown in Fig. 10(b). Initially, WFE is assumed to be ideal to show the effects of central obscuration. The central obstruction of the collimator is set to 100 mm. PSF ellipticity over full FOVs is obtained and compared with the results shown in Fig. 15(a). The variations of PSF ellipticity over full FOVs are obtained and shown in Fig. 16(a). Then, the central obstruction of the collimator is to be 150 mm, 200 mm, and 250 mm, PSF ellipticity errors over full FOVs are shown in Figs. 16(b)–16(d), respectively. Table 3 lists PSF ellipticity measurement errors of the collimator with different center obstruction radiuses. Obviously, center obstruction of the collimator has big effects on PSF ellipticity. What is more, PSF ellipticity measurement errors caused by central obstructions vary at different FOVs. If the central obstruction radius increases from 100 mm to 250 mm, the average and maximum measurement errors of PSF ellipticity increase gradually. According to Table 3, the average measurement errors are 2.29e-3, 2.75e-3, 3.17e-3, and 5.56e-3, and the maximum variances are 0.0074, 0.0091, 0.0110, and 0.0227.

In fact, collimators must contain certain WFE. The influences of central obscuration and WFE of collimators on PSF ellipticity measurement should be analyzed simultaneously. The RMS WFE of the obscured collimator shown

in Fig. 10(b) is set to 20 nm (its wavefront distribution results shown in Fig. 14). The radius of the central obstruction is 100 mm. In this case, PSF ellipticity over full FOVs is obtained, whose differences with the results shown in Fig. 15(b) are shown in Fig. 17(a). Similarly, the radius of the central obstruction is changed to be 150 mm, 200 mm, and 250 mm, respectively, PSF ellipticity measurement errors over full FOVs are shown in Figs. 17(b)–17(d), which are consistent with these shown in Figs. 16(a)–16(d). According to Table 3, if the central obstruction radius increases from 100 mm to 250 mm, the average and maximum measurement errors of PSF ellipticity increase gradually when the WEF RMS of the collimator is 20 nm. Moreover, the average errors are 3.20e-3, 4.72e-3, 7.00e-3, and 1.15e-2, and the maximum variances are 0.0136, 0. 0204, 0.0270, and 0.0457.

V. DISCUSSIONS AND CONCLUSION

PSF ellipticities of telescopes depends on many factors, such as optical design, manufacturing errors, optical alignment, and so on. There are big differences between the actual performances of PSF ellipticity of telescopes with those in design status. To ensure the used telescopes to be competent in WL detections and obtain PSF ellipticities of telescopes and their distribution characteristics over full FOVs, it is necessary to accurately measure PSF ellipticities of telescopes on the ground. According to the error budget of our telescope, measurement errors of PSF ellipticity should be smaller than 0.01. In this paper, a method based on simulated star target imaging is proposed to measure PSF ellipticity for an unobstructed off-axis space telescope. Related errors are identified and modeled. Effects of detector noises, micro-vibration of optical platforms, defocusing of simulated star target, WFEs and central obstructions of collimators on PSF ellipticity measurements of the telescope are analyzed. The following conclusions can be drawn:

(1) Lower centroid positioning errors are helpful to more accurate PSF ellipticity measurements. Several centroiding algorithms are involved and compared, the iterative weighted centroiding algorithm is chosen. 10 iterations are adopted when applying the iterative weighted centroiding algorithm. When SNR is 24 dB, the centroid positioning errors in x and y directions are reduced to be 4.78e-2 and 4.83e-2, respectively, resulting in PSF ellipticity measurement error being 4.32e-3.

(2) The effects of micro-vibration angles of optical platforms on PSF ellipticity measurements are analyzed at several FOVs. It is found that PSF ellipticity measurement errors at the marginal FOVs are greater than those at the center FOV. The maximum measurement error of PSF ellipticity is less than 0.01 if the micro-vibration angle of the optical platform can be control to be smaller than $0.05''$. At present, the micro-vibration angles of the optical platform are less than $0.02''$ in our lab, which can meet the accuracy requirement of the PSF ellipticity measurement.

(3) A collimator with a longer focal length is desirable to achieve small PSF ellipticity measurement errors. Considering several factors including control ability of defocusing of simulated star target, manufacture, alignment, and maintenance, a collimator that is twice the focal length of the telescope is chosen. The measurement error of PSF ellipticity is under 0.01 if the defocusing of simulated star target is not larger than 0.1 mm.

(4) The WFE and central obstruction of the collimator would alter PSF ellipticity measurement results of the telescope, and the differences induced by them vary at different FOVs. The maximum error of PSF ellipticity over full FOVs caused by RMS WFE of 20 nm of the collimator is 0.1, and the average value is 0.0269. The first 36 terms of Zernike aberrations, astigmatism and coma contribute mostly to PSF ellipticity measurement errors, especially higher-order astigmatism and coma. PSF ellipticity are affected by defocusing only at the marginal FOVs. It should be noted that the measurement errors of PSF ellipticity surpass 0.01 when the RMS WFE of the collimator is larger than 3 nm. Of course, if astigmatism and coma can be well limited, the requirements of the collimator WFE can be much looser than 3nm. Moreover, a larger central obstruction makes greater measurement error of PSF ellipticity. When the RMS WFE of the collimator is 0 nm, the maximum variance of PSF ellipticity is 0.0091 caused by a central obscuration radius of 150 mm, which meets the accuracy requirement. If the RMS WFE of the collimator is 20 nm, the maximum error becomes 0.0204. On the one hand, we should choose collimators carefully and improve the ability to accurately obtain the WFEs of collimators. On the other hand, the WFEs and central obscurations should be balanced when obscured collimator is used.

According to the results shown in this paper, some critical references to measure PSF ellipticities of astronomical telescopes in terms of detector noise suppression, micro-vibration of optical platforms, and selection of collimators are provided.

REFERENCES

[1] P. Schneider, "Detection of (dark) matter concentrations via weak gravitational lensing," *Monthly Notices Roy. Astronomical Soc.*, vol. 283, no. 3, pp. 837–853, Dec. 1996.

[2] R. Mandelbaum, C. M. Hirata, M. Ishak, U. Seljak, and J. Brinkmann, "Detection of large-scale intrinsic ellipticity—Density correlation from the Sloan Digital Sky Survey and implications for weak lensing surveys," *Monthly Notices Roy. Astronomical Soc.*, vol. 367, no. 2, pp. 611–626, Apr. 2006.

[3] M. J. Jee, R. L. White, H. C. Ford, G. D. Illingworth, J. P. Blakeslee, B. Holden, and S. Mei, "Weak-lensing detection at z ∼ 1.3: Measurement of the two lynx clusters with the advanced camera for surveys," *Astrophys. J.*, vol. 642, no. 2, p. 720, 2006.

[4] L. M. Lubin and A. Sandage, "The Tolman surface brightness test for the reality of the expansion. III. Hubble space telescope profile and surface brightness data for early-type galaxies in three high-redshift clusters," *Astronomical J.*, vol. 122, no. 3, pp. 1071–1083, Sep. 2001.

[5] N. Kaiser, G. Squires, and T. Broadhurst, "A method for weak lensing observations," *Astrophys. J.*, vol. 449, pp. 460–475, Nov. 1995.

[6] M. A. Troxel and M. Ishak, "The intrinsic alignment of galaxies and its impact on weak gravitational lensing in an era of precision cosmology," *Phys. Rep.*, vol. 558, pp. 1–59, Feb. 2015.

[7] C. Heymans, L. Van Waerbeke, D. Bacon, J. Berge, G. Bernstein, E. Bertin, S. Bridle, M. L. Brown, D. Clowe, H. Dahle, and T. Erben, "The shear testing programme 1: Weak lensing analysis of simulated ground-based observations," *Monthly Notices Roy. Astronomical Soc.*, vol. 368, no. 3, pp. 1323–1339, 2006.

[8] R. W. Besuner, M. J. M. J. Sholl, M. D. Lieber, and M. L. Kaplan, "Integrated modeling of point-spread function stability of the SNAP telescope," *Proc. SPIE*, vol. 6687, Sep. 2007, Art. no. 66870X.
[9] B. Lee, R.-R. Chary, and E. L. Wright, "Galaxy ellipticity measurements in the near-infrared for weak lensing," *Astrophys. J.*, vol. 866, no. 2, p. 157, Oct. 2018.
[10] A. M. Di Giorgio, P. Bastia, S. J. Liu, G. Giusi, R. Scaramella, M. Cropper, R. Cole, A. James, J. Amiaux, and Y. Mellier, "The command and data processing unit of the Euclid visible imager: Impact of the data compression needs on the unit design," *Proc. SPIE*, vol. 8442, Sep. 2018, Art. no. 844233.
[11] S. A. Johnson, M. Penny, B. S. Gaudi, E. Kerins, N. J. Rattenbury, A. C. Robin, S. Calchi Novati, and C. B. Henderson, "Predictions of the nancy grace Roman space telescope galactic exoplanet survey. II. Free-floating planet detection rates," *Astronomical J.*, vol. 160, no. 3, p. 123, Aug. 2020.
[12] M. Lacy, J. A. Surace, D. Farrah, K. Nyland, J. Afonso, W. N. Brandt, D. L. Clements, C. D. P. Lagos, C. Maraston, J. Pforr, and A. Sajina, "A Spitzer survey of deep drilling fields to be targeted by the vera C. Rubin observatory legacy survey of space and time," *Monthly Notices Roy. Astronomical Soc.*, vol. 501, no. 1, pp. 892–910, Dec. 2020.
[13] Y. Gong, X. Liu, Y. Cao, X. Chen, Z. Fan, R. Li, X.-D. Li, Z. Li, X. Zhang, and H. Zhan, "Cosmology from the Chinese space station optical survey (CSS-OS)," *Astrophys. J.*, vol. 883, no. 2, p. 203, Oct. 2019.
[14] A. Amara and A. Réfrégier, "Optimal surveys for weak-lensing tomography," *Monthly Notices Roy. Astronomical Soc.*, vol. 381, no. 3, pp. 1018–1026, Oct. 2007.
[15] C. Chang, S. M. Kahn, J. G. Jernigan, J. R. Peterson, Y. AlSayyad, Z. Ahmad, J. Bankert, D. Bard, A. Connolly, R. R. Gibson, and K. Gilmore, "Spurious shear in weak lensing with the large synoptic survey telescope," *Monthly Notices Roy. Astronomical Soc.*, vol. 428, no. 3, pp. 2695–2713, Jan. 2013.
[16] S. Paulin-Henriksson, A. Amara, L. Voigt, A. Refregier, and S. L. Bridle, "Point spread function calibration requirements for dark energy from cosmic shear," *Astron. Astrophys.*, vol. 484, no. 1, pp. 67–77, Jun. 2008.
[17] C. A. Hébert, B. Macintosh, and P. R. Burchat, "Characterization of atmospheric turbulence for the large synoptic survey telescope," *Proc. SPIE*, vol. 10700, Jul. 2018, Art. no. 107005E.
[18] M. Gentile, F. Courbin, and G. Meylan, "Interpolating point spread function anisotropy," *Astron. Astrophys.*, vol. 549, p. A1, Jan. 2013.
[19] M. J. Jee and J. A. Tyson, "Toward precision LSST weak-lensing measurement. I. Impacts of atmospheric turbulence and optical aberration," *Publications Astronomical Soc. Pacific*, vol. 123, no. 903, pp. 596–614, May 2011.
[20] R. Massey, H. Hoekstra, T. Kitching, J. Rhodes, M. Cropper, J. Amiaux, D. Harvey, Y. Mellier, M. Meneghetti, L. Miller, S. Paulin-Henriksson, S. Pires, R. Scaramella, and T. Schrabback, "Origins of weak lensing systematics, and requirements on future instrumentation (or knowledge of instrumentation)," *Monthly Notices Roy. Astronomical Soc.*, vol. 429, no. 1, pp. 661–678, Feb. 2013.
[21] X. Zhang, J. Zhang, G. Shi, Y. Wu, L. Wang, F. Zeng, H. Qu, J. Zhang, H. Wu, Y. Zhu, and C. Wang, "Optical design of off-axis astronomical space telescope based on freeform surfaces," *Proc. SPIE*, vol. 9293, Dec. 2013, Art. no. 92930P.
[22] J. Luo, X. He, K. Fan, and X. Zhang, "Effects of polarization aberrations in an unobscured off-axis space telescope on its PSF ellipticity," *Opt. Exp.*, vol. 28, no. 25, pp. 37958–37970, 2020.
[23] F. Zeng, X. Zhang, J. Zhang, G. Shi, and H. Wu, "Optics ellipticity performance of an unobscured off-axis space telescope," *Opt. Exp.*, vol. 22, no. 21, pp. 25277–25285, 2014.
[24] F. Li, X. Hu, and Q. Sun, "Estimating the PSF of space camera based on in-orbit wavefront sensing," *Proc. SPIE*, vol. 9623, Aug. 2015, Art. no. 96230A1.
[25] A. Karcher, C. J. Bebek, W. F. Kolbe, D. Maurath, V. Prasad, M. Uslenghi, and M. Wagner, "Measurement of lateral charge diffusion in thick, fully depleted, back-illuminated CCDs," *IEEE Trans. Nucl. Sci.*, vol. 51, no. 5, pp. 2231–2237, Oct. 2004.
[26] P. Z. Takacs, I. Kotov, J. Frank, P. O'Connor, V. Radeka, and D. M. Lawrence, "PSF and MTF measurement methods for thick CCD sensor characterization," *Proc. SPIE*, vol. 7742, Jul. 2010, Art. no. 774207.
[27] C. Bodendorf, N. Geis, F. Grupp, J. Kaminski, R. Katterloher, and R. Bender, "Testing the near-infrared optical assembly of the space telescope Euclid," *Proc. SPIE*, vol. 11116, Sep. 2019, Art. no. 111160Y.
[28] M. I. Andersen and A. N. Sorensen, "An interferometric method for measurement of the detector MTF," *Exp. Astron.*, vol. 8, no. 1, pp. 9–12, 1998.
[29] Y. Okura, K. Umetsu, and T. Futamase, "A method for weak-lensing flexion analysis by the HOLICs moment approach," *Astrophys. J.*, vol. 680, no. 1, pp. 1–16, Jun. 2008.
[30] Y. Okura and T. Futamase, "Elliptical-weighted HOLICs for weak lensing shear measurement. II. Point-spread function correction and application to a370," *Astrophys. J.*, vol. 748, pp. 1–10, Mar. 2012.
[31] Y. Okura and T. Futamase, "A new weak lensing shear analysis method using ellipticity defined by 0th order moments," *Astron. Astrophys.*, vol. 576, no. A63, pp. 1–8, 2015.
[32] Y. Okura and T. Futamase, "Analytical noise bias correction for weak lensing shear analysis with ERA," *Monthly Notices Roy. Astronomical Soc.*, vol. 479, no. 4, pp. 4971–4983, Oct. 2018.
[33] M. Born and W. Emil, *Principles of Optics*. Cambridge, U.K.: Cambridge Univ. Press, Oct. 1999.
[34] M. Bartelmann and P. Schneider, "Weak gravitational lensing," *Phys. Rep.*, vol. 340, nos. 4–5, pp. 291–472, 2001.
[35] J. Amiaux, J. L. Auguères, O. Boulade, C. Cara, S. Paulin-Henriksson, A. Réfrégier, S. Ronayette, A. Amara, A. Glauser, C. Dumesnil, A. M. Di Giorgio, J. Booth, M. Schweitzer, R. Holmes, M. Cropper, E. Atad-Ettedgui, L. Duvet, and D. Lumb, "Euclid imaging channels: From science to system requirements," *Proc. SPIE*, vol. 7731, Aug. 2010, Art. no. 77311I1.
[36] R. R. Shannon, *The Art and Science of Optical Design*. Cambridge, U.K.: Cambridge Univ. Press, Jun. 1997.
[37] B. Lindner, J. Garcia-Ojalvo, A. Neiman, and L. Schimansky-Geier, "Effects of noise in excitable systems," *Phys. Rep.*, vol. 392, no. 6, pp. 321–424, 2004.
[38] Y. Zhang, J. Jiang, G. Zhang, and Y. Lu, "Accurate and robust synchronous extraction algorithm for star centroid and nearby celestial body edge," *IEEE Access*, vol. 7, pp. 126742–126752, 2019.
[39] D. X. D. Yang and A. El Gamal, "Comparative analysis of SNR for image sensors with enhanced dynamic range," *Proc. SPIE*, vol. 3649, pp. 197–211, Apr. 1999.
[40] N. Hagen and E. L. Dereniak, "Gaussian profile estimation in two dimensions," *Appl. Opt.*, vol. 47, no. 36, pp. 6842–6851, 2008.
[41] P. M. Salomon, "Charge-coupled device (CCD) trackers for high-accuracy guidance applications," *Opt. Eng.*, vol. 20, no. 1, Feb. 1981, Art. no. 201135.
[42] Z. W. Chen, X. Wen, and D. J. Chen, "Application research for super-Gaussian random vibration test control strategy," *Appl. Mech. Mater.*, vol. 141, pp. 83–87, Nov. 2011.
[43] C. Li, X. He, Q. Ji, X. Zhang, and K. Fan, "Theoretical and experimental study on the testing accuracy of the image stabilization system of a space astronomical telescope," *Appl. Opt.*, vol. 59, no. 22, pp. 6658–6670, 2020.
[44] S. B. Hutchison, A. Cochrane, and S. McCord, "Updated status and capabilities for the LOTIS 6.5 meter collimator," *Proc. SPIE*, vol. 7106, Oct. 2008, Art. no. 710618.
[45] P. A. Sergeev, M. M. Miroshnikov, V. P. Zakharenkov, and A. S. Petropavlovsky, "Large optical test facility 'vertical' for space telescopes testing," *Proc. SPIE*, vol. 2199, pp. 1046–1051, Jun. 1994.
[46] P. A. Sergeev, Y. A. Gogolev, V. V. Zvonkova, I. R. Kobozev, S. V. Ostapenko, Y. R. Malamed, and V. V. Demidov, "Collimator equipment of the large optical test facility vertical for testing space telescopes," *Proc. SPIE*, vol. 2478, pp. 348–358, Jun. 1995.
[47] R. M. Bell, G. C. Robins, C. Eugeni, G. Cuzner, S. B. Hutchison, S. H. Baily, B. Ceurden, J. Hagen, K. Kenagy, H. M. Martin, M. Tuell, M. Ward, and S. C. West, "LOTIS at completion of collimator integration," *Proc. SPIE*, vol. 7017, Jul. 2008, Art. no. 7017D.
[48] F. Yang, M. Ming, F. Wang, L. Zhang, B. Chen, and L. Shao, "Conceptual design of 1.5 m aperture vertical collimator assembly with short tube and long focus," *Proc. SPIE*, vol. 8907, pp. 165–189, Sep. 2013.
[49] B. P. Holden1, M. Franx, G. D. Illingworth, M. Postman, A. van der Wel, D. D. Kelson, J. P. Blakeslee, H. Ford, R. Demarco, and S. Mei, "The ellipticities of cluster early-type galaxies from z $\sim$ 1 to z $\sim$ 0: No evolution in the overall distribution of bulge-to-disk ratios," *Astrophys. J.*, vol. 693, no. 1, p. 617, 2009.
[50] J. E. Harvey and F. Christ, "Diffraction effects of telescope secondary mirror spiders on various image-quality criteria," *Appl. Opt.*, vol. 32, no. 28, pp. 6337–6349, 1995.

KUO FAN received the B.S. degree in electro-optical engineering from Changchun University of Science and Technology. She is currently pursuing the Ph.D. degree with Changchun Institute of Optics, Fine Mechanics and Physics, Chinese Academy of Sciences, China. Her research interests include PSF ellipticity measurements and related errors analysis of space telescopes.

JING LUO received the B.S. degree from Changchun University of Science and Technology and the Ph.D. degree from Zhejiang University. He is currently working at Changchun Institute of Optics, Fine Mechanics and Physics, Chinese Academy of Sciences, China. His research interests include optical alignment technology and polarization aberration of space telescope.

XU HE is currently a Research Fellow and a Supervisor of M.S. candidates at Changchun Institute of Optics, Fine Mechanics and Physics, Chinese Academy of Sciences, China. His research interests include optical alignment technology and mechanical structure design.

CHENGHAO LI received the B.S. degree from Changchun University and the Ph.D. degree from Changchun Institute of Optics, Fine Mechanics and Physics, Chinese Academy of Sciences, China. He is currently working at Changchun Institute of Optics, Fine Mechanics and Physics, Chinese Academy of Sciences. His research interest includes image stabilization test of large-aperture camera.

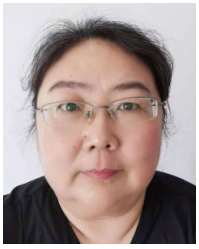

XIAOHUI ZHANG is currently a Research Fellow and a Supervisor of Ph.D. candidates at Changchun Institute of Optics, Fine Mechanics and Physics, Chinese Academy of Sciences, China. Her research interests include optical detection and image quality evaluation technology.